

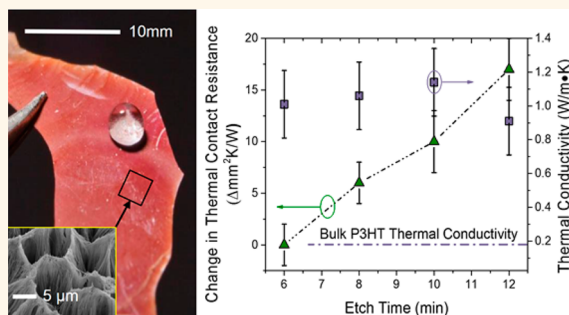
Poly(3-hexylthiophene) Nanotube Array Surfaces with Tunable Wetting and Contact Thermal Energy Transport

Matthew K. Smith,[†] Virendra Singh,[‡] Kyriaki Kalaitzidou,^{†,‡} and Baratunde A. Cola^{*,†,‡}

[†]School of Materials Science and Engineering and [‡]George W. Woodruff School of Mechanical Engineering, Georgia Institute of Technology, Atlanta, Georgia 30332, United States

ABSTRACT Solution casting using a sacrificial template is a simple technique to fabricate vertical arrays of polymer nanotubes. However, because of their close proximity and high aspect ratios, large capillary forces cause nanotubes to cluster as the array dries; researchers often use special drying techniques to avoid this clustering. Here, we exploit the clustering of regioregular poly(3-hexylthiophene) (rr-P3HT) nanotubes in a unique template etching process to create surfaces that exhibit tunable wetting and contact thermal energy transport. Vertical arrays of rr-P3HT nanotubes are cast from solution in nanoscale alumina templates, and a solution etching process is used to partially release the nanotubes from the template.

The clustering of rr-P3HT nanotube tips upon template etching produces hierarchical surface structuring with a distinct pattern of interconnected ridges, and the spacing between the ridges increases with increased template etch times. These changes in morphology cause the water contact angle to increase from 141° to 168° as the etch time is increased from 4 to 12 min. When assembled into an interface, the morphological changes cause the thermal contact resistance of the vertical rr-P3HT nanotube arrays to increase linearly at a rate of approximately 6 mm² · K/W per 2 min etch interval (after 6 min of etching is surpassed). The effective thermal conductivity of the rr-P3HT nanotube arrays is 1 ± 0.2 W/mK independent of the etch time, which is approximately 5 times higher than the bulk rr-P3HT film value.



KEYWORDS: nanotube · wetting · hydrophobic · thermal · tunable · interface

High aspect ratio, polymer nanotubes (PNTs) and nanowires exhibit remarkable electrical,^{1–4} thermal,^{5–10} and mechanical^{11–13} properties that are attributed to preferential chain alignment and high surface area to volume ratios. Moreover, polymers can be processed quickly at low temperatures, offering the potential of inexpensive, high-throughput manufacturing.¹⁴ These traits make solution-processed polymer nanotubes interesting for many potential commercial applications. For example, polythiophene nanotube array thermal interface materials⁹ (TIMs) and polyethylene nanowire arrays^{10,15} that exhibit dramatically improved anisotropic thermal conductivity were recently reported, and there have been multiple reports on the use of vertically aligned, high-aspect-ratio polymer nanotubes to create surfaces with superhydrophobic and tunable wetting properties.^{15–19} This study investigates the thermal transport and wetting properties of the polythiophene

derivative regioregular poly(3-hexylthiophene) (rr-P3HT) PNT arrays. We choose this polymer because rr-P3HT is stable at high temperatures and can undergo solvation in organic solvents (solution processing) at room temperature, but is stable in aqueous environments.⁹ These qualities make rr-P3HT ideal for harsh, high-temperature environments of which TIMs are commonly exposed and the stability in aqueous solutions is also important for microfluidic applications. In addition, rr-P3HT is commercially available and is commonly used in organic electronic devices, but much less work has been done to investigate thermal transport properties.

For both wetting and thermal interface applications, nanotube arrays are often grown on a substrate where the bottom of the array is anchored and the other end consists of free tips. Because of the wet processing conditions and because the densely packed tubes have high aspect ratios, the vertical arrays have the tendency to

* Address correspondence to cola@gatech.edu.

Received for review May 20, 2014 and accepted January 13, 2015.

Published online January 13, 2015
10.1021/nn5027406

© 2015 American Chemical Society

bundle and aggregate during processing through elastocapillary coalescence.^{15,16,19–24} Elastocapillary coalescence occurs when capillary forces cause objects to elastically bend into contact with each other upon which the objects stick together through adhesion. Nanotube aggregation can dramatically alter the surface morphology and the corresponding interactions between the PNT array and a contacting liquid or substrate. For example, capillary effects can result in a surface with microstructures comprising smaller nanostructures, achieving a hierarchical arrangement similar to surfaces often found in nature and that are known to display special wettability.^{15,25,26} Although nanotube array surface morphology has been proven to influence surface wetting properties,^{18,19,24,27–29} we find no prior reports that correlate the degree of aggregation to the contact thermal energy transport of PNT array interfaces. Understanding this relationship is critical because, despite their high intrinsic thermal conductivities, thermal contact resistance (TCR) has been a major limitation of high aspect ratio structures such as carbon nanotube (CNT) array TIMs.^{30–32} In addition, the favorable mechanical properties and strong adhesion of soft materials,¹³ as compared to CNTs, further supports the hypothesis that PNTs could potentially reduce the high contact resistance associated with traditional nanotube interfaces. However, prior methods to fabricate high aspect ratio nanostructures with tunable surface morphology, and thus surface properties, are still relatively complex,^{18,19,24,27–29} often relying on lithographic processes, special drying conditions, or varying structure dimensions, so there is a need to develop simple approaches.

Here, we replicate a simple solution-based nanoporous template wetting technique^{33–35} to fabricate rr-P3HT nanotube arrays, but modify the template etching process to easily alter the array surface

morphology as a function of released nanotube length. Distinct surface morphologies are then characterized by measuring their surface fractions and the surface fractions are correlated to the wetting and thermal transport properties. Additionally, the water contact angle (WCA) and contact angle hysteresis (CAH) are measured and array surface fractions are used to compare the measured surface wetting behavior to the theoretical Cassie–Baxter relationship.³⁶ In order to elucidate the relationship between array morphology and TCR, the photoacoustic method³⁰ (PA) is used to measure the change in the TCR as a function of the surface fraction. The PA technique is also used to measure array thermal conductivity as a function of morphology and to measure the improvement in thermal conductivity due to nanoscale confinement.

RESULTS AND DISCUSSION

Fabrication and Structure of PNT Arrays with Tunable Surface Morphologies.

A solution consisting of 2 mg/mL rr-P3HT dissolved in chlorobenzene was cast onto 60 μm thick nanoporous anodic aluminum oxide (AAO) templates with an estimated porosity of 40–50% and rated nominal pore diameter of 200 nm. The polymer solution infiltrated the nanopores spontaneously driven by wetting phenomena,³³ and the solvent was removed in ambient conditions through evaporation (Figure 1a step 1). After solvent evaporation, the infiltrated AAO–polymer composite structures were exposed to a 1 M KOH solution to remove the alumina and partially free the nanotubes (Figure 1a step 2). Partial template etching was achieved by placing a small drop on the surface of the AAO and therefore only exposing one side of the template to etchant. The resulting nanotubes had 150–300 nm diameters with wall thicknesses ranging from 20 to 40 nm; their exact geometries vary due to template inconsistencies (Figure S1,

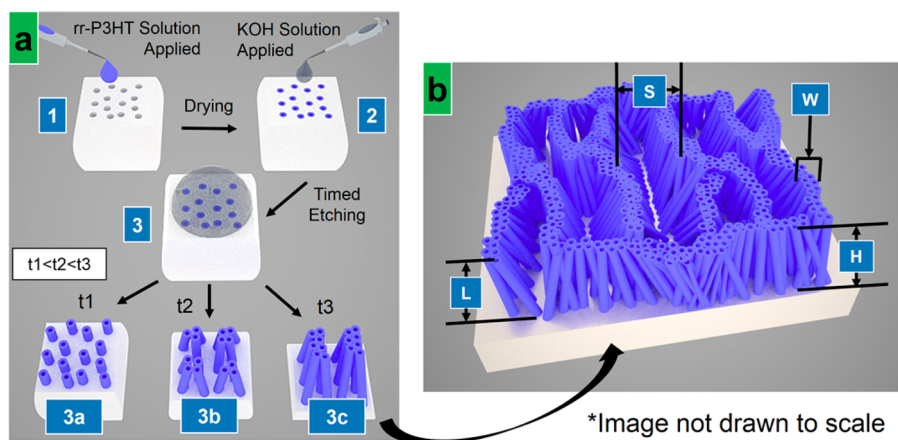


Figure 1. Solution process to fabricate arrays of vertically aligned polymer nanotubes and nanotube bundles. In step 1 of panel a, the AAO nanoporous template is wetted with rr-P3HT solution. After drying, KOH is pipetted on top of the template to begin the top-down template etching process (step 3). For steps 3a, 3b, and 3c, the increase in bundle size as the etch time increases from t_1 to t_3 is illustrated. Panel b highlights the formation of ridges for large surface area, densely packed nanopolymer arrays where S is the spacing between ridges, L is the nanotube length, H is the array height, and W is the ridge width.

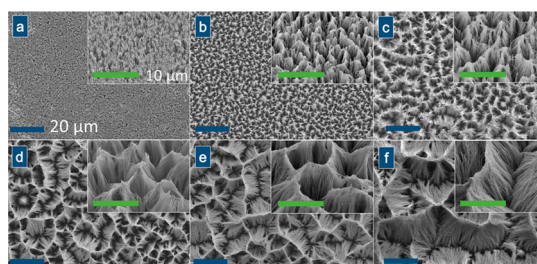


Figure 2. Scanning electron micrographs a–f represent the change in the surface morphology as the AAO etch time increases from 2 to 12 at 2 min intervals, respectively. The insets show the corresponding surfaces at an increased magnification. Scale bar 20 μm (inset 10 μm).

Supporting Information). The longer the etch time, the greater the length of exposed nanotube and degree of nanotube clustering (Figure 1a step 3a–c).

When the process in Figure 1 is applied to large area, high-density arrays of PNTs, interconnected ridges form that exhibit a constant width (W) (width becomes constant after 6 min of etching). However, the characteristic spacing between ridges (S) increases dramatically as the exposed nanotube length increases (Figure S2, Supporting Information). In contrast to prior studies that focus on the nanostructure bundle size,^{27,28} we found that the ridge spacing directly relates to the surface fraction, which can be used to estimate wettability, assuming Cassie–Baxter behavior.³⁶ To fabricate several surfaces with unique and reproducible surface fractions, the etch time was varied from 2 to 12 at 2 min intervals. By placing the etchant drop so that it only contacted the top surface of the template we were able to precisely control the length of freed nanotubes and the corresponding surface morphology of the PNT array (Figure 2a–f).

As the etch time is increased, the length of the exposed nanotubes and the degree of capillary driven bundling increases, resulting in distinct ridge formation. The ridging effect occurs when the elastocapillary forces pull the nanotubes together, and once capillary forces are not present (i.e., after evaporation of the wetting agent), the nanotube clusters are preserved through intertube adhesion.²⁹ The initial clustering (of individual PNTs) and then subsequent bundling of clusters into ridges is driven by an imbalance between the bending stiffness of the PNTs and the capillary force that arises between PNTs, where the capillary force is greater than the nanotube bending stiffness. The capillary force is driven by the intramolecular forces between the liquid and the PNT surface (due to the interfacial surface energy) and the surface tension of the liquid. As etch time increases, the relative stiffness of the PNTs and PNT clusters is reduced allowing for increased deformation. For vertically aligned nanotube arrays, the relationship between nanotube length (L) and the number of nanotubes per bundle (N) has been approximated using a force balance eq 1 where the

number of nanotubes in a discrete cluster is a function of the cube of the nanotube length and is inversely related to the Young's modulus.^{27,29}

$$N \approx \frac{E_C}{E_E} \approx \frac{\gamma_{la} L^3 \cos^2 \theta_0}{D(p - D)^2 E} \quad (1)$$

In eq 1, E_C is the capillary interaction energy, E_E is the elastic energy of the tube, γ_{la} is the surface tension between the liquid and air, D is the diameter of the tube, p is the distance between the tubes, θ_0 is the equilibrium contact angle of a liquid on the surface of the tubes, E is the tube's Young's Modulus, and L is the nanotube length. In the present experiment the nanotube length changes significantly as etch time increases, and consequently, tube clustering is predicted to increase dramatically due to the corresponding reduction in stiffness. However, instead of the discrete clusters predicted in eq 1 and observed in previous studies,^{27,29} percolating ridges of PNTs form, a close examination of Figure 2 reveals that these ridges are present even at the shorter etch times (inset of Figure 2b). Equation 1 predicts extremely large cluster sizes (Figure S2, Supporting Information) and is not valid for this type of material system. For example, we used eq 1 and a range of nanotube elastic moduli values to predict the degree of clustering for the 8 min etched sample and found that the predicted bundle size is nearly 15,000 nanotubes for an assumed moduli of 1 GPa³⁷ (Figure S3, Supporting Information). Although the percolating ridges could contain this large number of tubes, the surface clearly has much finer features as illustrated in the inset of Figure S3, Supporting Information. We attribute the deviation from predicted clustering behavior at increased aspect ratios to the relatively low elastic modulus of polymer nanotubes as similar behavior has been observed in other high aspect ratio systems.³⁸

We found that the surface fraction of the PNT array decreases as etch time and ridge formation increases, in contrast to earlier studies that have found an increase in surface fraction with increasing Cu and Si nanowire bundling.^{18,27,28} For etch times of 6 min and longer, there is no measurable change in the width of the PNT ridges, while the spacing between the ridges increases considerably (Figure 3). Here, we use a SEM contrasting method²⁷ to determine the surface fraction, f , as a function of etch time where heavily contrasted images were used to attain pixel counts for the ridged regions only. In Figure 3a–d, the ridges were traced to clearly illustrate ridge widening as the etch time increases from 6 to 12 min, respectively, and Figure 3e–h shows the corresponding percolation ridge traces. The surface fraction, f , is reduced from 0.20 ± 0.02 for the 6 min etch time to a minimum of 0.06 ± 0.01 for the 12 min etch time. The relationship between etch time and surface fraction appears to be nonlinear since the magnitude of change in surface

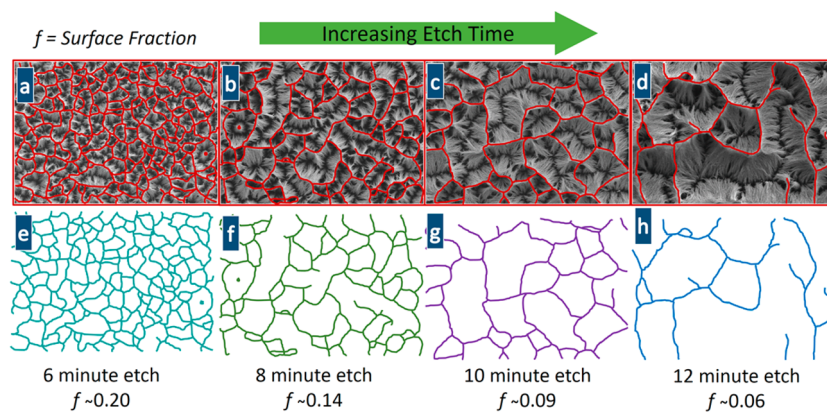


Figure 3. Scanning electron micrographs (a–d) illustrate the ridge tracing method as the etch time increased from 6 to 12 at 2 min intervals, respectively. Images e–h demonstrate the corresponding ridge trace areas and their calculated surface fractions, f .

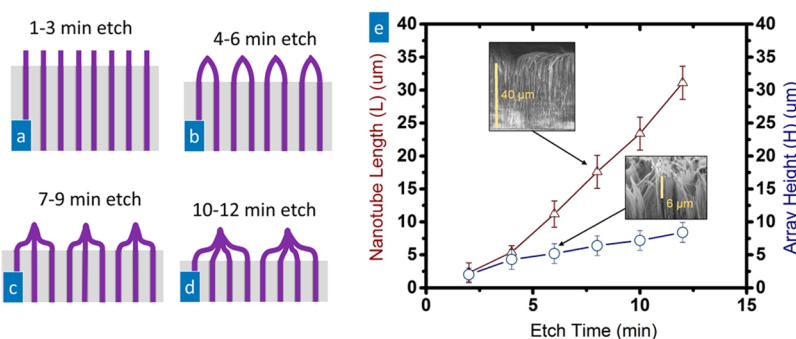


Figure 4. Illustrations a–d represent a simple model used to explain the formation of ridges and the increase in spacing between ridges with increasing etch times. Graph e illustrates the relationship between the length of exposed nanotube and the array height as the etch time increases. The blue circles represent H and correspond to the array height axis, whereas the red triangles represent L and correspond to the nanotube length axis. The top inset depicts a cross-sectional measurement of the template thickness after 8 min of etching, and the lower inset is a cross sectional measurement of the nanotube array height after 6 min of etching. H and L were measured at 10 different locations along the sample cross section, and the uncertainty is a measure of the standard deviation of those measurements.

fraction decreases with etch time (Figure S4). The measurement uncertainty was found by calculating the standard deviation of 10 measurements, 5 different spots on 2 separate samples with similar etch times. We used the measured values and eq 1 to introduce a simple semiempirical expression (Equation S1, Supporting Information) to estimate the resulting surface fraction for the 6, 8, 10, and 12 min etched samples (Figure S5, Supporting Information).

Figure 4 illustrates a simple model to explain the morphological changes the surfaces undergo due to alterations to the partially released nanotube length. As the etch time increases, the length of exposed nanotube increases, and the elastic force required to bend the nanotubes is reduced.²³ At the early stages of the etching process, the nanotube tips bend together, and wide ridges form where the tip clusters are joined (Figure 4b). As the etch time increases further, the ridges continue to add additional nanotubes, and they become more densely packed forming sharp ridge peaks (Figure 4c). The sharp ridges grow further apart and eventually begin to flatten and collapse into each other as they become more isolated (Figure 4d).

Throughout the etching process the relationship between array height (H) and the nanotube length (L) (Figure 1b) is also changing and as shown in Figure 4e. As the etch time increases at discrete 2 min increments, the exposed nanotube length increases nearly linearly and the thickness of the etched alumina template decreases with time (at a rate of approximately $6 \mu\text{m}$ per 2 min interval). Conversely, the array height first increases significantly and then begins to plateau, and further etching past the 12 min mark will eventually produce a collapsed mat of PNTs (Figure S6, Supporting Information). Cross-sectional SEMs of the etched AAO templates (Figure 4e insets) were used to measure the change in nanotube array height and nanotube length. The height of exposed PNTs was also measured with tapping mode atomic force microscopy (Figure S7, Supporting Information) to confirm estimates from SEMs.

Surface Wetting Behavior of Vertically Aligned PNT Arrays.

In general, surface wetting properties depend on the surface texturing and the intrinsic wetting properties of the material. If a smooth surface exhibits a contact angle (CA) greater than 90° , then the Cassie–Baxter

(CB) model may predict the apparent CA of the textured version of this surface using the resulting surface fraction, f .³⁶ The apparent CA of the textured surface can be substantially larger than the smooth surface CA because the wetting fluid may rest upon the surface peaks with air pockets trapped between the peaks and below the fluid. For example, after etching of 4 min or longer, we observed contact angles greater than 150° and posit that the wetting fluid rests on top of a composite surface consisting of rr-P3HT ridges and air. However, this wetting behavior was only observed after thermal treatment of the nanotube arrays (templates were placed on a hot plate at 250 °C with the exposed nanotubes facing up for 10 s and then rapidly cooled under ambient conditions), otherwise the surface contact angle is $\sim 0^\circ$.

The thermally induced transition from wetting to nonwetting is likely due to thermal reconstruction effects where the polymer chains at the nanotube surface undergo accelerated compositional or conformational changes.³⁹ The nanotube surface will accumulate polar species as the *n*-hexyl side chains and sulfur species undergo radical oxidation in air upon drying.^{40,41} However, thermodynamically driven diffusion and chain conformational changes may redistribute the polar species away from the surface during heating rendering the surface more hydrophobic. Therefore, the observed improvement in hydrophobicity suggests that the heating conditions used leads to molecular reorganization at the surface without reintroducing a significant level of surface oxidation. To support this we measured the contact angle of films processed under nitrogen atmosphere ($102^\circ \pm 2^\circ$) and films fabricated under ambient conditions ($94^\circ \pm 2^\circ$) where partial oxidation is expected. The contact angle of the partially oxidized films is near the 90° boundary between being hydrophobic and hydrophilic, and this may explain the dramatic shift in nanotube wettability after heating. In addition, a change in the mechanical properties of the surface structures that prevents the release of capillary driven ridging upon rewetting may also contribute to the improved hydrophobicity.²⁹ This change in surface mechanics may be attributed to a change in polymer crystallinity, which could enhance the tubes elastic modulus,⁴² or lead to a nanotube welding phenomena where the intertube adhesion is improved due to partial sintering. The surfaces were imaged before and after thermal treatment, and there was no detectable change in morphology, so the wetting transition is likely a direct result of the thermal reconstruction, the thermal sintering effect, or a combination of both.

The CA of a DI water drop on a smooth rr-P3HT film processed under nitrogen atmosphere measured $\sim 102^\circ$, whereas the CA for 8 to 12 min etched rr-P3HT nanotube arrays measured greater than 150°. The CA variations of a CB wetting system are dependent upon the surface

fraction and can be described by³⁶

$$\cos(\theta^*) = -1 + f(\cos(\theta_0) + 1) \quad (2)$$

where θ^* is the apparent CA that results from structuring, θ_0 is the contact angle on a smooth surface, and f is the surface fraction. However, it is important to note that this model is rather simplistic and other explanations for surface wetting are introduced below. Another important wetting property is the contact angle hysteresis (CAH), which is a measurement of the difference between the advancing contact angle (ACA) and receding contact angle (RCA) (CAH = ACA – RCA) (Figure S8, Supporting Information). The CAH quantifies the adhesiveness of a surface to a wetting fluid; the larger the CAH, the more adhesive the surface is to that fluid.³⁶ The CA and the CAH as a function of template etch time as well as the CA values predicted using the CB model (using the experimentally determined surface fractions and the measured rr-P3HT film CA of 102°) are shown in Figure 5. The CA for the 2 min etched surface is not included in Figure 5 because it was the only surface to demonstrate a contact angle well below the bulk P3HT film CA of $\sim 102^\circ$. This finding suggests that the CA of the 2 min etched surface is biased by wetting fluid interactions with the hydrophilic AAO surface.

A surface is superhydrophobic when its CA is greater than 150° and CAH is less than or equal to 10°. ⁴³ As shown in Figure 5, the surfaces associated with 8, 10, and 12 min etch times can be classified as superhydrophobic, where the maximum contact angle

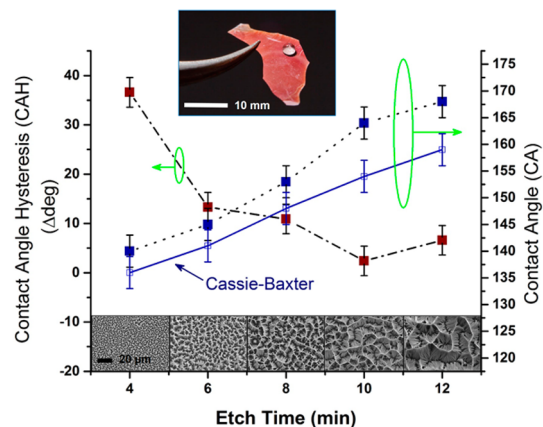


Figure 5. Top inset shows the superhydrophobicity exhibited by the 10 min etched surface. The graph depicts the surface wetting properties as a function of increasing etch time from 4 to 12 min. The red squares correspond to the contact angle hysteresis (CAH) axis, the blue squares correspond to the contact angle (CA) axis, and the solid blue line with open squares represents the theoretical CB contact angle calculated using the measured surface fractions and the intrinsic CA of 102° and also corresponds to the CA axis. The inset images along the x-axis illustrate the changing surface morphology as the etch time increases from 4 to 12 at 2 min intervals. The measurement uncertainty was derived from the standard deviation of 9 total measurements where 3 measurements were taken at three different spots on the sample surface.

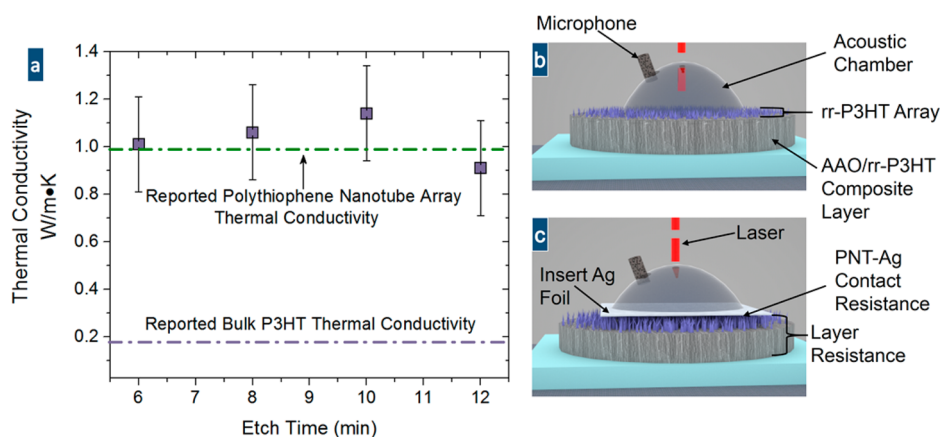


Figure 6. Graph a shows that as the etch time increases from 6 to 12 min the array thermal conductivity (indicated by the purple square markers) remains nearly constant within the range of uncertainty (see Figures S11 and S12 and Table S2, Supporting Information for uncertainty, sensitivity, and data fitting details, respectively). Illustrations b and c show the photoacoustic array thermal conductivity and interface resistance measurement assemblies, respectively.

achieved is nearly 170° for the 12 min etch time, and the lowest hysteresis is less than 5° for the 10 min etch time. The CA results correlate well to the Cassie–Baxter relation; a small surface fraction produces a large CA and a large surface fraction produces a smaller CA. The largest deviations from the model occur at the lowest surface fractions (i.e., longest etch times), but even at these values the experimental results are within 10° of the calculated values. The deviation from the CB model is likely due to the partial oxidation of the nanotube surfaces, uncertainty in measuring the true surface fraction and intrinsic CA, and shortcomings of the CB model. The validity of the CB model is a current point of debate in the literature and works by Gao and McCarthy^{44,45} and Extrand⁴⁶ suggest that the model fails to accurately predict the apparent contact angle on a textured surface. In particular, the CB model fails to accurately predict CA and CAH when applied to surfaces with spatially heterogeneous asperities and recent works have attempted to modify the CB model for improved robustness.⁴⁷ However, an elementary CB comparison is useful here because it validates the predicated interaction between the surface and droplet and demonstrates the impact of inhomogeneous surfaces.

Thermal Contact Resistance and Thermal Conductivity of Vertically Aligned PNT Arrays. We used the photoacoustic (PA) method to determine the array thermal conductivity, and the thermal contact resistance (TCR) between the tips of the rr-P3HT nanotubes and a surface as a function of the etch time. The PA method is a well-accepted technique to measure the thermal properties of nanostructured materials.^{30,48} In brief, the PA method works by heating the sample with a modulated laser and measuring the acoustic response in a chamber that is sealed atop the sample. The chamber is often pressurized with helium to increase the signal strength and to control contact pressure in an interface.³⁰ More details on the PA method are

in the Supporting Information and our prior work.^{30,49} Our recent modification to the PA method⁹ is used to measure the rr-P3HT array thermal conductivities (Figures 6 and S9, Supporting Information). The sample configuration for measuring the array thermal conductivity is shown in Figure 6b, where the nanotube array is exposed directly to the PA laser to increase the sensitivity of the measurement to array thermal conductivity (Figure S10, Supporting Information).⁹

The measured thermal conductivity of the rr-P3HT nanotube arrays is approximately $1 \text{ W/m}\cdot\text{K}$, independent of etch time (Figure 6a). These results are similar to the thermal conductivities reported for polythiophene nanotube arrays made through electropolymerization using the same nanoporous alumina templates.⁹ Using the template porosity of $\sim 50\%$ reported by the manufacturer, we estimate the thermal conductivity of individual rr-P3HT nanotubes to be $\sim 2 \text{ W/m}\cdot\text{K}$, which is about an order of magnitude higher than the reported bulk film value⁵⁰ and agrees well with the reported thermal conductivity of melt processed semicrystalline P3HT nanowires with similar diameters.⁵¹ Directional chain alignment has been shown to enhance thermal conductivity in amorphous polymer nanostructures,⁹ and crystallinity may also improve thermal transport.⁵¹ Therefore, the results of the present work suggest that anisotropic chain alignment is promoted in this system as well because the rr-P3HT nanotubes appear to be amorphous from electron diffraction analysis on several samples (Figure S1c, Supporting Information).

In order to isolate the impact of the surface fraction on thermal transport, the total thermal resistance of the rr-P3HT nanotube array–AAO template composites in contact with silver foil (inset of Figure 7) was measured as a function of etch time (Figure 7). Since the array thermal conductivity does not change with etch time (Figure 6a) and thermal transport through the composite AAO/rr-P3HT layer is limited by contact

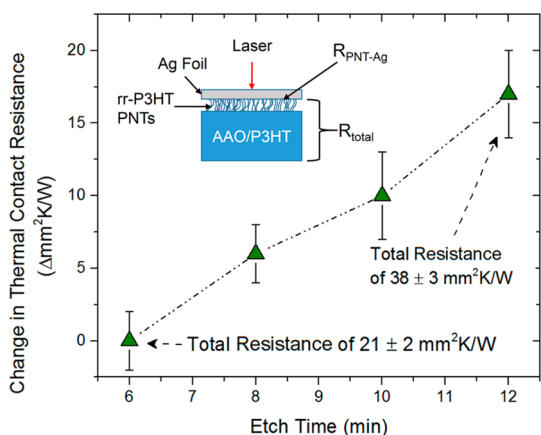


Figure 7. Total thermal interface resistance, which is the measured sum of the resistance between the PNT tips and the silver foil ($R_{\text{PNT-AG}}$), the layer resistance of the nanotube array, the PNT–AAO composite layer resistance, and the interface resistance between the nanotubes and the composite structure, for the surfaces with 6, 8, 10, and 12 min etch times is indicated by the green line with triangular markers. Each data point represents the average of three measurements taken at different spots on the surface. The photoacoustic fitting parameters and a representative data fit and sensitivity plots are included in the Supporting Information Table S3 and Figures S13–S15, respectively.

resistance between the template walls and the part of the nanotubes that is still in the template (i.e., the path of least thermal resistances is from the tip to the base of the PNTs), the change in total thermal resistance is likely dominated by the change in the PNT–Ag contact resistance. The reported total resistance value corresponds to the sum of the resistance between the PNT tips and the silver foil ($R_{\text{PNT-AG}}$), the layer resistance of the nanotube array, the PNT–AAO composite layer resistance, and the interface resistance between the nanotubes and the composite structure.

The total thermal resistance was measured after 6 min of etching and Figure 7 shows the relationship between etch time and the change in $R_{\text{PNT-AG}}$, determined by subtracting the total resistance for the surfaces with 8, 10, and 12 min etch times from the total resistance of the surface after 6 min of etching. One potential artifact of this type of measurement is that the surface fraction may be changing during photoacoustic testing due to compression forces (the silver foil placed onto the PNT surfaces is under 138 kPa). However, the sample surface undergoes no noticeable change in morphology when imaged after testing, and any surface fraction change due to normal compression is expected to be similar for all samples. If bending of the ridges occurs, we do not expect the degree of bending to be significant because the ridge formation distributes the load over the entire array resulting in a high effective resistance to bending, and any increase in surface fraction is expected to scale based on the initial fraction, similar to the scaling expected for normal compression.

As the etch time increases, the total thermal resistance increases from the initial minimum of $21 \pm 2 \text{ mm}^2 \cdot \text{K/W}$ measured after an etch time of 6 min to a final value of $38 \pm 3 \text{ mm}^2 \cdot \text{K/W}$ measured for the 12 min etch time at a rate of approximately $6 \text{ mm}^2 \cdot \text{K/W}$ per 2 min interval. The increase in thermal resistance is due to a decrease in the number of nanotube tips in contact with the surface and possibly due to a slight decrease in the array thermal conductivity as nanotubes collapse and lose their vertical alignment. We note that the collapse of nanotubes decreases the thickness of the sample (i.e., the exposed array plus the remaining template), which likely reduces the combined layer resistances with increased etch times. Thus, the increase in contact resistance with etch time is likely even larger than what can be concluded directly from the measurements of total thermal resistance. The resistance values for the 2 and 4 min etched samples were not measured due to template and etching inconsistencies including height variations that could lead to artificially high contact resistance values.

CONCLUSIONS

We developed a two-step solution processing technique to fabricate vertically aligned arrays of regioregular poly(3-hexylthiophene) nanotubes with tunable surface morphologies and thus tunable properties, including wetting (contact angle and contact angle hysteresis) and thermal contact resistance as two important candidate applications. The surface morphologies are dictated by the length of nanotubes freed in a template etching process, with longer etch times resulting in larger exposed lengths, larger spacing between the nanotube surface ridges, and smaller surface fractions, in contrast to prior reports of increased surface fractions with capillary bundling of vertical nanowires.^{18,27,28} The self-assembled poly(3-hexylthiophene) nanotube array surfaces roughly follow Cassie–Baxter wetting trends and are superhydrophobic with static contact angles greater than 150° and contact angle hysteresis less than or equal to 10° when the surface fraction is below 0.15. The total thermal resistance of an interface assembled with the poly(3-hexylthiophene) nanotube arrays increases from a minimum of $21 \pm 2 \text{ mm}^2 \cdot \text{K/W}$ to a maximum of $38 \pm 3 \text{ mm}^2 \cdot \text{K/W}$ as the etch time increased from 6 to 12 min, which is likely caused by the reduction in surface fraction and contact area at the interface. The thermal conductivity of the poly(3-hexylthiophene) nanotube arrays is 5-fold larger than the bulk film value because of molecular chain alignment in the direction of heat transfer, which enables the material to produce very low thermal transport resistances for a pure polymer. Our results demonstrate the achievement of tunable superhydrophobic surfaces through a novel solution processing method and illustrate the impact of array morphology on the thermal contact

resistance of vertically aligned, high aspect ratio polymer nanostructures, which could emerge as tunable

materials to meet the needs of a variety of important applications.

MATERIALS AND METHODS

Nanotube Fabrication. Anodic aluminum oxide templates (AAO) purchased from Whatman were used to fabricate polymer nanotube arrays through the template solution wetting method described. Regioregular (with regioregularity = 98%), average $M_n = 87,000$, poly(3-hexylthiophene) (P3HT) was purchased from Sigma-Aldrich (445703-1G) and was used as received. A solution of rr-P3HT (2 mg/mL) in chlorobenzene was used for the template wetting method. The AAO templates were placed on a clean glass slide and then 2 μL of solution was pipetted on top of each template. After placing the solution onto the template, a second glass slide was used to sandwich the templates and create an even distribution of solution. The top slide was removed after sandwiching, and the solvent was allowed to evaporate in a chemical hood. After drying overnight, potassium hydroxide (KOH) was used to selectively remove the AAO template to reveal free-standing rr-P3HT nanotube arrays as depicted in Figure 1. Following the designated etching time, the samples were rinsed five times in a bath of DI water to remove any excess KOH. After rinsing, the composites were placed on clean glass slides to dry.

Structural Characterization. A Zeiss scanning electron microscope at 5 kV was used to determine the characteristic spacing between nanotube peaks, the degree of percolation, and the exposed nanotube length. The array height and the surface fraction were found using a Dimension 3100 scanning probe microscope (SPM) that utilizes automated atomic force microscopy (AFM) in tapping mode. In order to measure wall thickness, the AAO templates were completely removed, and a centrifuge was used to transfer the free nanotubes into a container of water. The nanotube solution was then cast onto grids, and a JEOL 100CX II transmission electron microscope operated at 100 kV was used to confirm the formation of nanotubes as opposed to nanowires and to measure the tube diameter, wall thickness, and to perform diffraction analysis (Figure S1, Supporting Information).

Characterization of Surface Wetting. Both the CA and CAH were measured by dispensing a 2 μL drop of deionized water onto the PNT surface (Figure S7, Supporting Information) with a Rame-Hart Model 250 Standard Goniometer. For the advancing and receding contact angle measurements, the dispensing needle was placed near the sample surface, and the CA was measured as excess fluid was dispersed (advancing CA) and then measured again as the fluid was retracted (receding CA). The CAH was found by taking the difference in the receding and advancing CA.

Thermal Transport Measurements. The thermal properties were measured using the photoacoustic method where a 1 mm diameter pulsed laser was used to periodically heat the surface of a sample enclosed in a pressured helium chamber. The heat is conducted into the sample and upward into the helium gas resulting in periodic pressure fluctuations. The pressure fluctuations induce acoustic waves and the acoustic wave amplitude, and the phase is measured using a microphone. The sample configuration for the array thermal conductivity and interface resistance measurements are illustrated in Figure S8, Supporting Information. For each measurement, the sample phase was compared to a reference of known properties (80 nm of Ti on a quartz slide), and the measured phase shifts, along with initial guess values for unknown properties, were used in a theoretical model to estimate the thermal properties of the samples (Tables S2 and S3, Supporting Information).

Conflict of Interest: The authors declare the following competing financial interest(s): Georgia Tech has applied for a patent, application no. PCT/US 61/484,937, related to the design methods and materials produced in this work.

Supporting Information Available: Additional structural characterization results, predictions of surface fraction using a

modified force balance equation, detailed images of the methods used to measure the water contact angle and contact angle hysteresis, and a more in-depth explanation of the photoacoustic thermal measurements and sensitivity analysis. This material is available free of charge via the Internet at <http://pubs.acs.org>.

Acknowledgment. This work was supported by the National Science Foundation (NSF; grant no. CBET-1133071) and an NSF-IGERT graduate fellowship for M.K.S.

REFERENCES AND NOTES

- Martin, C. R. Membrane-Based Synthesis of Nanomaterials. *Chem. Mater.* **1996**, *8*, 1739–1746.
- Martin, C. R. Template Synthesis of Electronically Conductive Polymer Nanostructures. *Acc. Chem. Res.* **1995**, *28*, 61–68.
- Duvail, J. L.; Retho, P.; Fernandez, V.; Louarn, G.; Molinie, P.; Chauvet, O. Effects of the Confined Synthesis on Conjugated Polymer Transport Properties. *J. Phys. Chem. B* **2004**, *108*, 18552–18556.
- Shirai, Y.; Takami, S.; Lasmono, S.; Iwai, H.; Chikyow, T.; Wakayama, Y. Improvement in Carrier Mobility of Poly(3,4-Ethylenedioxythiophene) Nanowires Synthesized in Porous Alumina Templates. *J. Polym. Sci., Part B: Polym. Phys.* **2011**, *49*, 1762–1768.
- Choy, C. L.; Fei, Y.; Xi, T. G. Thermal-Conductivity of Gel-Spun Polyethylene Fibers. *J. Polym. Sci., Part B: Polym. Phys.* **1993**, *31*, 365–370.
- Shen, S.; Henry, A.; Tong, J.; Zheng, R.; Chen, G. Polyethylene Nanofibres with Very High Thermal Conductivities. *Nat. Nanotechnol.* **2010**, *5*, 251–255.
- Wang, X.; Ho, V.; Segalman, R. A.; Cahill, D. G. Thermal Conductivity of High-Modulus Polymer Fibers. *Macromolecules* **2013**, *46*, 4937–4943.
- Fujishiro, H.; Ikebe, M.; Kashima, T.; Yamanaka, A. Thermal Conductivity and Diffusivity of High-Strength Polymer Fibers. *Jpn. J. Appl. Phys., Part 1* **1997**, *36*, 5633–5637.
- Singh, V.; Bougher, T. L.; Weathers, A.; Cai, Y.; Bi, K.; Pettes, M. T.; McMenamin, S. A.; Lv, W.; Resler, D. P.; Gattuso, T. R.; et al. High Thermal Conductivity of Chain-Oriented Amorphous Polythiophene. *Nat. Nanotechnol.* **2014**, *9*, 384–390.
- Cao, B. Y.; Li, Y. W.; Kong, J.; Chen, H.; Xu, Y.; Yung, K. L.; Cai, A. High Thermal Conductivity of Polyethylene Nanowire Arrays Fabricated by an Improved Nanoporous Template Wetting Technique. *Polymer* **2011**, *52*, 1711–1715.
- Smith, P.; Lemstra, P. J. Ultra-High-Strength Polyethylene Filaments by Solution Spinning/Drawing. *J. Mater. Sci.* **1980**, *15*, 505–514.
- Papkov, D.; Zou, Y.; Andalib, M.; Goponenko, A.; Cheng, S.; Dzenis, Y. Simultaneously Strong and Tough Ultrafine Continuous Nanofibers. *ACS Nano* **2013**, *7*, 3324–3331.
- Lu, G.; Hong, W.; Tong, L.; Bai, H.; Wei, Y.; Shi, G. Drying Enhanced Adhesion of Polythiophene Nanotubule Arrays on Smooth Surfaces. *ACS Nano* **2008**, *2*, 2342–2348.
- Tadmor, Z.; Gogos, C. G. Injection Molding. In *Principles of Polymer Processing*; John Wiley & Sons: New York, 2006.
- Cao, B.-Y.; Kong, J.; Xu, Y.; Yung, K.-L.; Cai, A. Polymer Nanowire Arrays with High Thermal Conductivity and Superhydrophobicity Fabricated by a Nano-Molding Technique. *Heat Transfer Eng.* **2013**, *34*, 131–139.
- Jin, M.; Feng, X.; Feng, L.; Sun, T.; Zhai, J.; Li, T.; Jiang, L. Superhydrophobic Aligned Polystyrene Nanotube Films with High Adhesive Force. *Adv. Mater.* **2005**, *17*, 1977–1981.
- Mao, C.; Liang, C.; Luo, W.; Bao, J.; Shen, J.; Hou, X.; Zhao, W. Preparation of Lotus-Leaf-Like Polystyrene Micro- and Nanostructure Films and Its Blood Compatibility. *J. Mater. Chem.* **2009**, *19*, 9025–9029.

18. Liao, Y. C.; Chiang, C. K.; Lu, Y. W. Contact Angle Hysteresis on Textured Surfaces with Nanowire Clusters. *J. Nanosci. Nanotechnol.* **2013**, *13*, 2729–2734.
19. Xu, J.; Li, M.; Zhao, Y.; Lu, Q. Control over the Hydrophobic Behavior of Polystyrene Surface by Annealing Temperature Based on Capillary Template Wetting Method. *Colloids Surf., A* **2007**, *302*, 136–140.
20. Li, H.; Wang, X.; Song, Y.; Liu, Y.; Li, Q.; Jiang, L.; Zhu, D. Super-"Amphiphobic" Aligned Carbon Nanotube Films. *Angew. Chem., Int. Ed.* **2001**, *40*, 1743–1746.
21. Bico, J.; Roman, B.; Moulin, L.; Boudaoud, A. Adhesion: Elastocapillary Coalescence in Wet Hair. *Nature* **2004**, *432*, 690.
22. Arezki, B.; José, B.; Benoît, R. Elastocapillary Coalescence: Aggregation and Fragmentation with a Maximal Size. *Phys. Rev. E: Stat., Nonlinear, Soft Matter Phys.* **2007**, *76*, 060102.
23. Hill, J.; Haller, K.; Gelfand, B.; Ziegler, K. Eliminating Capillary Coalescence of Nanowire Arrays with Applied Electric Fields. *ACS Appl. Mater. Interfaces* **2010**, *2*, 1992–1998.
24. Duan, H.; Berggren, K. Directed Self-Assembly at the 10 Nm Scale by Using Capillary Force-Induced Nanocoherence. *Nano Lett.* **2010**, *10*, 3710–3716.
25. Barthlott, W.; Neinhuis, C. Purity of the Sacred Lotus, or Escape from Contamination in Biological Surfaces. *Planta* **1997**, *202*, 1–8.
26. Feng, L.; Zhang, Y.; Xi, J.; Zhu, Y.; Wang, N.; Xia, F.; Jiang, L. Petal Effect: A Superhydrophobic State with High Adhesive Force. *Langmuir* **2008**, *24*, 4114–4119.
27. Dawood, M. K.; Zheng, H.; Kurniawan, N. A.; Leong, K. C.; Foo, Y. L.; Rajagopalan, R.; Khan, S. A.; Choi, W. K. Modulation of Surface Wettability of Superhydrophobic Substrates Using Si Nanowire Arrays and Capillary-Force-Induced Nanocoherence. *Soft Matter* **2012**, *8*, 3549–3557.
28. Indrani, C.; Neha, S.; Smita, G.; Shankar, G.; Pushan, A. Clustered Copper Nanorod Arrays: A New Class of Adhesive Hydrophobic Materials. *Soft Matter* **2013**, *9*, 11513–11520.
29. Kang, S.; Pokroy, B.; Mahadevan, L.; Aizenberg, J. Control of Shape and Size of Nanopillar Assembly by Adhesion-Mediated Elastocapillary Interaction. *ACS Nano* **2010**, *4*, 6323–6331.
30. Cola, B. A.; Xu, J.; Cheng, C. R.; Xu, X. F.; Fisher, T. S.; Hu, H. P. Photoacoustic Characterization of Carbon Nanotube Array Thermal Interfaces. *J. Appl. Phys.* **2007**, *101*, 054313.
31. Taphouse, J. H.; Smith, O. N. L.; Marder, S. R.; Cola, B. A. A Pyrenylpropyl Phosphonic Acid Surface Modifier for Mitigating the Thermal Resistance of Carbon Nanotube Contacts. *Adv. Funct. Mater.* **2014**, *24*, 465–471.
32. Tao, T.; Yang, Z.; Lance, D.; Ali, K.; Meyyappan, M.; Arun, M. Dense Vertically Aligned Multiwalled Carbon Nanotube Arrays as Thermal Interface Materials. *IEEE Trans. Compon., Packag., Manuf. Technol.* **2007**, *30*, 92–100.
33. Steinhart, M.; Wendorff, J.; Greiner, A.; Wehrspohn, R.; Nielsch, K.; Schilling, J.; Choi, J.; Gösele, U. Polymer Nanotubes by Wetting of Ordered Porous Templates. *Science* **2002**, *296*, 1997.
34. Steinhart, M.; Wehrspohn, R.; Gösele, U.; Wendorff, J. Nanotubes by Template Wetting: A Modular Assembly System. *Angew. Chem., Int. Ed.* **2004**, *43*, 1334–1344.
35. Schlitt, S.; Greiner, A.; Wendorff, J. H. Cylindrical Polymer Nanostructures by Solution Template Wetting. *Macromolecules* **2008**, *41*, 3228–3234.
36. Gennes, F.; D; A; B Capillarity and Wetting Phenomena: Drops, Bubbles, Pearls, Waves. *Phys. Today* **2004**, *57*, 120000–120067.
37. Shanmugham, S.; Jeong, J.; Alkhateeb, A.; Aston, E. D. Polymer Nanowire Elastic Moduli Measured with Digital Pulsed Force Mode Afm. *Langmuir* **2005**, *21*, 10214–10218.
38. Chakrapani, N.; Wei, B.; Carrillo, A.; Ajayan, P. M.; Kane, R. S. Capillarity-Driven Assembly of Two-Dimensional Cellular Carbon Nanotube Foams. *Proc. Natl. Acad. Sci. U.S.A.* **2004**, *101*, 4009–4012.
39. Holmes-Farley, S.; Reamey, R. H.; Nuzzo, R.; McCarthy, T. J.; Whitesides, G. M. Reconstruction of the Interface of Oxidatively Functionalized Polyethylene and Derivatives on Heating. *Langmuir* **1987**, *3*, 799–815.
40. Manceau, M.; Rivaton, A.; Gardette, J. L.; Guillerez, S.; Lemaitre, N. The Mechanism of Photo- and Thermooxidation of Poly(3-Hexylthiophene) (P3ht) Reconsidered. *Polym. Degrad. Stab.* **2009**, *94*, 898–907.
41. Jeong, M. G.; Seo, H. O.; Kim, D. H.; Kim, K. D.; Park, E. J.; Kim, Y. D.; Lim, D. C. Initial Stage of Photoinduced Oxidation of Poly(3-Hexylthiophene-2,5-Diyl) Layers on ZnO under Dry and Humid Air. *J. Phys. Chem. C* **2014**, *118*, 3483–3489.
42. Tan, E. P.; Lim, C. T. Effects of Annealing on the Structural and Mechanical Properties of Electrospun Polymeric Nanofibres. *Nanotechnology* **2006**, *17*, 2649–2654.
43. Wong, T.-S.; Sun, T.; Feng, L.; Aizenberg, J. Interfacial Materials with Special Wettability. *MRS Bull.* **2013**, *38*, 366–371.
44. Gao, L.; McCarthy, T. J. How Wenzel and Cassie Were Wrong. *Langmuir* **2007**, *23*, 3762–3765.
45. Gao, L.; McCarthy, T. J. An Attempt to Correct the Faulty Intuition Perpetuated by the Wenzel and Cassie "Laws". *Langmuir* **2009**, *25*, 7249–7255.
46. Extrand, C. W. Model for Contact Angles and Hysteresis on Rough and Ultraphobic Surfaces. *Langmuir* **2002**, *18*, 7991–7999.
47. Choi, W.; Tuteja, A.; Mabry, J. M.; Cohen, R. E.; McKinley, G. H. A Modified Cassie-Baxter Relationship to Explain Contact Angle Hysteresis and Anisotropy on Non-Wetting Textured Surfaces. *J. Colloid Interface Sci.* **2009**, *339*, 208–216.
48. Hanping, H.; Xinwei, W.; Xianfan, X. Generalized Theory of the Photoacoustic Effect in a Multilayer Material. *J. Appl. Phys.* **1999**, *86*, 3593.
49. Wang, X.; Cola, B. A.; Bougher, T. L.; Hodson, S. L.; Fisher, T. S.; Xu, X. Photoacoustic Technique for Thermal Conductivity and Thermal Interface Measurements. In *Annual Review of Heat Transfer*; Begell House, Inc: Danbury, CT, 2013; Vol. 16, pp 135–157.
50. Duda, J. C.; Hopkins, P. E.; Shen, Y.; Gupta, M. C. Thermal Transport in Organic Semiconducting Polymers. *Appl. Phys. Lett.* **2013**, *102*, 251912.
51. Rojo, M. M.; Martin, J.; Grauby, S.; Borca-Tasciuc, T.; Dilhaire, S.; Martin-Gonzalez, M. Decrease in Thermal Conductivity in Polymeric P3ht Nanowires by Size-Reduction Induced by Crystal Orientation: New Approaches Towards Thermal Transport Engineering of Organic Materials. *Nanoscale* **2014**, *6*, 7858–7865.